American Mineralogist, Volume 92, pages 603–616, 2007

Complexity in 15- and 30-sectors polygonal serpentine: Longitudinal sections, intrasector stacking faults and XRPD satellites

E. Mugnaioli,[1,*] M. Logar,[2] M. Mellini,[1] and C. Viti[1]

[1]Dipartimento di Scienze della Terra, Università di Siena, Via Laterina 8, 53100 Siena, Italy
[2]Department of Mineralogy, University of Belgrade, Djusina 7, Belgrade, Serbia and Montenegro

Abstract

Pale-green massive serpentine veins cutting the Yugoslavian serpentinites consist of 15- and 30-sectors polygonal serpentine in random orientation but becoming stress-oriented close to the vein walls. [100] cross-sections show ordered one-layer and two-layer projected polytype sequences, as well as disordered multilayer sequences. From sector to sector, these sections have systematically alternating polytypes that obey the O-L-R and O-R-L alternation rules in 15- and 30-sectors polygonal serpentine, respectively. Furthermore, [010] longitudinal sections systematically show a unique two-layer sequence. By combining the two projections, we reconstruct the basic 3D polytype assemblage that from sector to sector consists of alternating M5-M15-M15 or M5-M16-M16 polytypes.

The individual fibers may be described as cyclical pseudo-twins, based upon continuous 1:1 layers, with possible octahedral rotation from one sector to the other. Continuous curved sector boundaries join adjacent sectors, with no tetrahedral sheet inversion; the curved boundaries behave as similar folds and have variable interplanar spacings. Simulated electron diffraction patterns reproduce all the observed diffraction geometries, even for faulted stacking sequences, and explain numbers of diffraction cusps and chords. Additional XRPD reflections are indexed based on polytypes present in 15- and 30-sectors polygonal serpentines.

Keywords: Polygonal serpentine, polytypism, twinning, stacking faults, electron diffraction, HRTEM

Introduction

Pale-green splintery serpentine veins are common within massive serpentinites. Some consist of fibrous antigorite (e.g., Viti and Mellini 1996), others of fibrous serpentine with X-ray diffraction patterns akin to chrysotile. Eckhardt (1956) and Zussman and Brindley (1957) noticed rotational disorder lower than in chrysotile, as indicated by sharp X-ray diffraction spots in the even layers ($h = 2n$) of [100] fiber patterns, or by additional X-ray powder diffraction (XRPD) lines. This serpentine variety was initially named "Povlen-type" chrysotile (Krstanović 1967; Krstanović and Pavlović 1964). The names "schweizerite" (Eckhardt 1956; Zussman and Brindley 1957) or "chrysotiloid" (Varlakov and Guriev 1985; Podvysotskiy 1985) have also been used. Transmission electron microscopy (TEM) microstructural studies finally led to the name "polygonal serpentine" (PS), as [100] cross-sections showed polygonally arranged sectors, formed by flat 1:1 serpentine layers (Cressey and Zussman 1976; Middleton and Whittaker 1976; Cressey 1979; Jiang and Liu 1984; Mellini 1986; Yada and Wei 1987; Mitchell and Putnis 1988; Papp 1990).

The number of sectors matches the "magic numbers" 15 or 30 (hereafter PS-15 and PS-30, respectively), with sectors rotated by 24° or 12°. These values arise because, from the core to the rim, five b repeats are added each 1:1 layer; sectors will be 15 or 30, depending on the addition of **b**/3 or **b**/6 components at every intersector junction (Baronnet and Mellini 1992; Chisholm 1992; Baronnet et al. 1994; Cressey et al. 1994; Baronnet and Devouard 1996; Logar and Viti 1996; Dódony 1997a). Baronnet and Devouard (2005) showed that PS is made of laterally continuous 1:1 layers, with no tetrahedral inversion at the curved sector boundaries. Although different, this model is similar to those of Chisholm (sharp boundaries with no inversion) and Dódony (sharp boundaries with inversion). The basic features of the Baronnet and Devouard's model are the local, non-crystallographic fivefold axial symmetry and the concerted presence of specific polytypes in adjacent sectors. This model agrees with the Dódony's observations, as far as the alternation of three different oblique two-dimensional (2D) cells is concerned. From sector to sector, in [100] projections there is a one-layer orthogonal (O) cell, an oblique right-slanting (R) cell, and an oblique left-slanting (L) cell (being O-R-L and O-L-R the counterclockwise alternations in 30- and 15-sectors fibers, respectively).

In addition, we report [100] TEM data on nanostructure and polytypism in PS-15 and PS-30, comparing our results with the previous models. We also focus on complex [100] diffraction patterns, characterized by "wings," "cusp points," and "chords" (Baronnet and Devouard 2005), which we interpret as due to intrasector radial stacking faults.

Finally, we deal with [010] longitudinal sections, to understand the three-dimensional (3D) polytype arrangements. The resulting 3D polytype model is used to index additional reflections in the XRPD patterns.

* E-mail: mugnaioli4@unisi.it

0003-004X/07/0004–603$05.00/DOI: 10.2138/am.2007.2272

Samples and geological setting

Polygonal serpentine is widespread in all the serpentinites we have studied through the years (e.g., Viti and Mellini 1997; Rumori et al. 2004). For the present study, we selected specimens within an extensive collection of rocks from the Yugoslavian ophiolites (Logar 1992). All of them are massive pale-green serpentine veins, cutting the main serpentinite. Quite often, the veins show deformation features (folding and slickensides). Specimens were selected based upon their XRPD patterns, looking for the ones with the most evident additional reflections, namely reflections not present in the XRPD of chrysotile or lizardite.

S491 is a compact, pale-green serpentine vein from Kačanik (Crni Kamen). It is partially coated by umber limonite layers. Striated sharp parallel grooves and slickensides occur on the vein surface, due to intense tectonic movements and friction with the surrounding serpentinites. S491 has average chemical composition (Logar 1992)

$$(Mg_{2.83}\ Fe^{2+}_{0.08}\ Fe^{3+}_{0.03})\ (Si_{1.97}\ Al_{0.03})\ O_{4.90}\ (OH)_4.$$

According to Logar and Viti (1996), it consists of chrysotile 2*Mc*$_1$ and PS-30 fibers. This specimen was used for Rietveld X-ray refinement (Krstanović 1997); however, this result should be considered as a simplified partial substructure refinement, because it was obtained assuming just one polytype, common to all the sectors.

S265 is similar to S491 and comes from the serpentinized harzburgites outcropping on the northern slopes of Mt. Kopaonik, close to Josanicka Banja. The plastically deformed gray-greenish veins have average chemical composition of

$$(Mg_{2.72}\ Fe^{2+}_{0.03}\ Fe^{3+}_{0.23})\ (Si_{1.89}\ Al_{0.10})\ O_5\ (OH)_4.$$

S1279 and S1283 come from Mt. Korab and Mt. Nichpur serpentinites, close to the Macedonia-Albania border. Undeformed pale-green serpentine veins have average chemical composition of

$$(Mg_{2.95}\ Fe^{2+}_{0.02}\ Fe^{3+}_{0.03}\ Al_{0.02})\ (Si_{1.94}\ Al_{0.06})\ O_5\ (OH)_4.$$

Experimental methods

TEM specimens, extracted from thin sections cut perpendicular to the vein lineation, were thinned by Ar^+ ion milling (Gatan Dual Ion Mill). TEM was done using a JEOL 2010 microscope, working at 200 kV, equipped with LaB_6 source and ultra-high resolution (UHR) pole pieces capable of 0.19 nm point resolution. A TV-rate CCD camera with image amplifier was used for focus and astigmatism corrections. Electron images and selected area electron diffraction (SAED) patterns were recorded by either photographic films or imaging plates (Fuji film FDL5000, 3760 × 3000 pixels, 100 × 81 mm in size, 16384 gray levels), which allowed exposure times lower than 1 s and limited image drifting and beam damage.

Fast-Fourier Transform (FFT) and filtering were performed by the Fuji-LProcess software. FFTs were calculated from raw images selecting 256 × 256, 512 × 512 (1 sector) or 1024 × 1024 (two or more adjacent sectors) pixels wide areas. FFT filtering was performed by applying row-like masks, i.e. selecting 00*l*, 02*l* and $02\bar{l}$ diffraction rows in [100] projections and 00*l*, 20*l*, and $20\bar{l}$ diffraction rows in [010] projections, and suppressing the noise located close to the transmitted beam. Information-rich diffuse streaks (i.e., the diffuse streaks between 00*l* diffraction spots from adjacent sectors) were used in image reconstruction.

XRPD patterns have been collected using different preparation techniques (ground powders; rock chips, cut parallel or perpendicular to lineation) and two different diffractometers have been used (Philips PW 1051, operating with Ni-filtered Cu*K*α; Philips PW 1710, operating with post-diffraction graphite monochromator, 2θ step of 0.02°, counting time of 1 second per step).

Results

Overall TEM texture

All the specimens consist of PS and chrysotile (ctl) with no lizardite or antigorite. When cut perpendicular to the lineation, they predominantly show PS and ctl fiber cross-sections. The fibers have a common orientation close to the vein boundary, whereas they approach random texture in the inner vein (Figs. 1a and 1b, from PS-30 and PS-15, respectively). The shearing stress along the vein boundary affects the gliding surface by orienting the adjacent fibers, but with limited inward strain propagation. Similar PS random textures, coupled with local partially oriented regions, have been previously reported by Cressey (1979).

Whereas S491 and S265 consist of PS-30 only, S1279 and S1283 mostly consist of PS-15 with rare PS-30. Overall crystallinity (based upon PS/ctl ratio and fiber size) decreases from S491 to S265, and from S1279 to S1283. In S491, several ctl fibers occur together with large PS-30 fibers, producing a nanoporous, loose texture (Fig. 1a); in contrast, S1279 consists of smaller, irregular PS-15 fibers, with less ctl and a more compact texture (Fig. 1b).

In general, the fiber diameter is up to 600 nm in PS-30 and up to 400 nm in PS-15. Smaller partially polygonalized fibers (100–300 nm in diameter) appear as an intermediate, transitional structure between chrysotile and well-developed polygonal serpentine. In all the cases, the fiber length may reach 2 μm. PS-30 usually has a regular habit, with perfectly circular cross-sections (Fig. 1c); conversely, PS-15 often displays irregular indented cross-sections, with unequal growth in adjacent sectors and in-

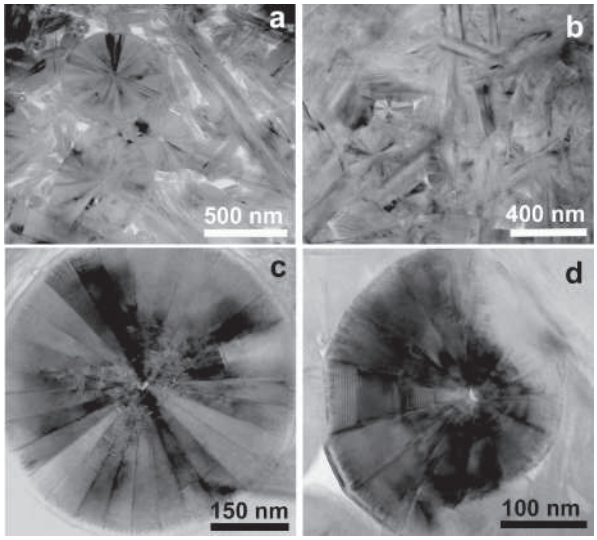

Figure 1. TEM images of PS-30 and PS-15, from specimens cut perpendicular to the vein lineation. (**a**) Low magnification image, showing the overall texture of PS-30 (S491). The smallest fibers are chrysotile. The vein texture is microporous. (**b**) Low magnification image, showing the non-porous texture of PS-15 (S1283). (**c**) PS-30 cross-section with regular habit (S491). (**d**) PS-15 cross-section with unequal growth in different sectors (S1283).

completely developed sectors (Fig. 1d), or with frequent chrysotile partial fibers at sector boundaries. We never observed single polygonal fibers with mixed 24° and 12° intersector rotations.

In contrast to what was reported in previous studies (e.g., Baronnet and Devouard 2005), our PS-15 and PS-30 fibers have large hollow cores, consisting of 5 or 6 deformed partial chrysotile fibers (Figs. 2a and 2b). Close to the core, the PS structure is deformed, with frequent disorder features such as anomalous layer curvature and disordered stacking sequences. PS becomes more regular toward the rim, where the polygonal sectors are well developed and separated by sharp boundaries.

In longitudinal sections, PS fibers display frequent indentations filled by ctl or poorly crystalline serpentine (Figs. 3a and 3b). These indentations are up to 200 nm deep in the outer sectors but leave the central core unaffected (e.g., the light-contrast core in Figs. 3a and 3b). Usually, indentations are limited by rough surfaces, variably oriented with respect to the [100] fiber axis. For properly oriented PS fibers, we measured recurrent angles of 114–116°, 102–105°, and 96–97° between (001) and indentations surfaces. In some cases, (001) lattice fringes propagate out from surfaces.

During observation, PS fibers suffer rapid beam damage, localized at three preferential sites: (1) PS cores, with beam-induced layer bending and parting; (2) intersector boundaries, with amorphization of intersector junctions; and (3) outermost PS fiber, with the development of a continuous amorphous ring 1–2 lattice fringes wide. These fringes have a periodicity larger than 7 Å and are possibly indicative of surface relaxation.

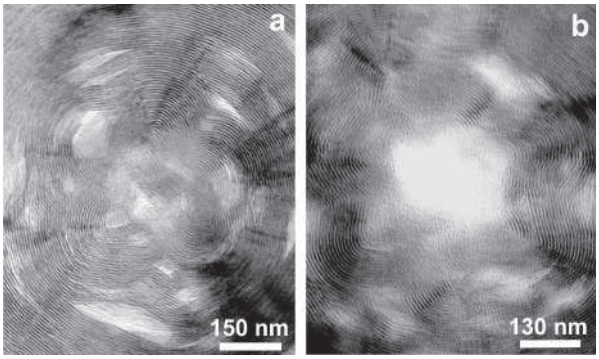

FIGURE 2. (**a**) and (**b**) [100] cross-sections of large, hollow cores in PS-30, showing 5 to 6 deformed partial chrysotile fibers (S491).

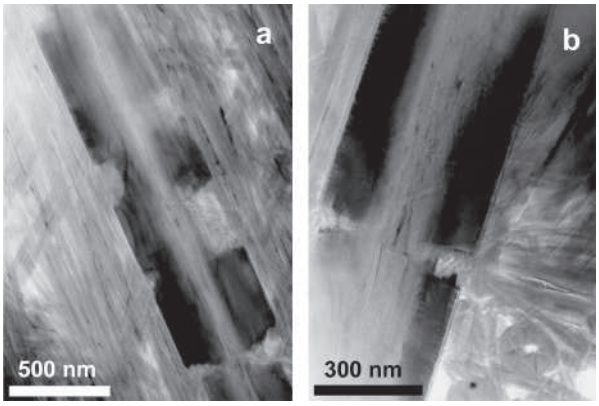

FIGURE 3. (**a**) and (**b**) [010] longitudinal sections of PS-15 (S1283) and PS-30 (S491), respectively. The two large PS fibers are intergrown with several other PS and chrysotile fibers. Strong contrast characterizes the inner core with respect to the outer sectors. The indentations in the fibers are filled by chrysotile.

[010] projections: HR images, Fourier-filtering, and SAED patterns

Whereas the [100] projection has been studied several times (e.g., Dódony 1997a; Baronnet and Devouard 2005), the [010] images and SAED patterns have been little studied. Thus, the current appraisal of PS polytypism suffers by missing one dimension and represents only projected polytype arrangements. We therefore collected longitudinal images and SAED patterns for both PS-15 and PS-30. This task is not easy, because of the severe overlap of adjacent sectors. Single-sector [010] images and SAED patterns were gathered by: (1) crystal tilt in phase-contrast mode, until a sharp contrast zoning was obtained (in particular, low contrast in PS core and dark contrast in the outer fiber); (2) use of smallest SAED aperture (sampling an area of 0.1 μm in diameter); (3) selection of the outer fiber; and (4) further crystal tilting in diffraction mode, to optimize orientation. When one sector was not obtained, the SAED pattern showed additional spots or whole diffraction rows in non-rational positions.

Experimental [010] SAED patterns. We collected more than twenty single-sector [010] SAED patterns for both PS-15 and PS-30. All are very similar, always showing two-layer oblique reciprocal cells, with β* close to 83° (Fig. 4). All the randomly sampled sectors, in both PS-15 and PS-30, have common [010] diffraction properties, independently from the actual [001] stacking sequence.

The 00*l* row and (when visible as in Fig. 4b) the 60*l* row show sharp, strong 7 Å spots, sometimes with weak 14 Å extra-reflections, interpreted as dynamical effects. In contrast, 20*l* and 40*l* rows show sharp 14 Å spots, that indicate projected two-layer polytypes. *h*0*l* rows with *h* odd are systematically absent, due to *C*-centering (i.e., *hkl* present for $h + k = 2n$). Even though accurate and precise d_{hkl} SAED measurements are difficult, the measurement of several patterns for both PS-15 and PS-30 revealed almost constant reciprocal spacing along [100]*, but slightly variable spacing along [001]*. Thus, we used d_{200} as an internal standard (2.67 Å is almost constant in serpentine) find-

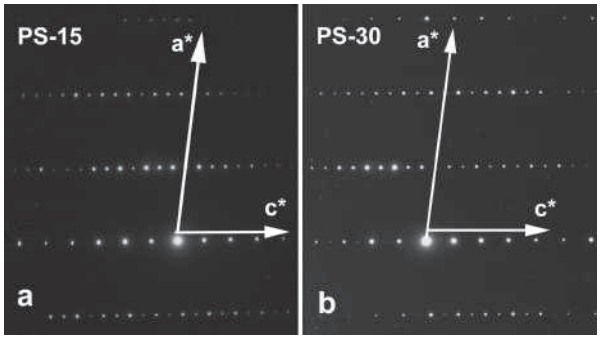

FIGURE 4. (**a**) Experimental [010] SAED pattern for PS-15 (S1283); (**b**) experimental [010] SAED pattern for PS-30 (S491). The two reciprocal lattices, based upon 14 Å periodicities, are indistinguishable.

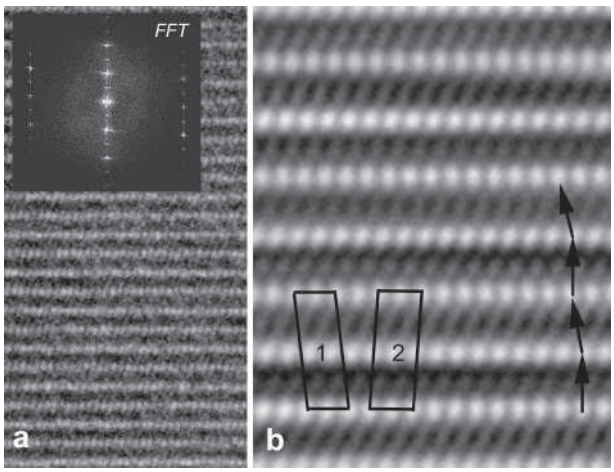

▲ **Figure 5.** (**a**) [010] lattice image of a PS-30 fiber (S491); the FFT (inset) shows 14 Å periodicity. (**b**) [010] Fourier-filtered image of **a**, showing the stacking sequence of 1:1 layers. Two possible projected unit cells are drawn (1 and 2); cell 1 was preferred because it corresponds to a pair of layers stacked directly one over the other, with adjacent pairs shifted by **a**/3.

ing d_{00l} spacings significantly larger in PS-15 than in PS-30; in particular, from d_{00l} = 7.38 Å to d_{00l} = 7.22 Å (14.76 and 14.44 Å for the two-layer polytypes), respectively.

[010] lattice images. Figure 5a is the experimental [010] image of a PS-30 fiber, with the corresponding FFT pattern (inset). In FFT, 00*l* row consists of strong 7 Å spots, with weaker 14 Å extra-reflections; the two-layer periodicity is evident in the 20*l* rows, characterized by similar 14 Å reflections. With respect to the corresponding experimental SAED pattern, the FFT emphasizes this periodicity. Figure 5b shows the corresponding Fourier-filtered image, characterized by rows of bright dots, separated by **a**/2 and regularly alternating to rows of gray dots. Adjacent layers are stacked by orthogonal vectors and by oblique vectors (see arrows in Fig. 5b). Two possible orientations of the oblique vector may be chosen, producing two different projected unit cells (1 and 2 in Fig. 5b). The first setting was preferred, because

▼ **Figure 6.** [100] projection of a PS-30 fiber consisting of projected one-layer ordered polytypes (S491). (**a**) experimental lattice image, with L-O-R counterclockwise polytype alternation. The FFTs of the three adjacent L, O, and R sectors are shown in the insets; (**b**) Fourier-filtered images of the three adjacent L, O, and R sectors; the three **c** vectors (vertical arrows) are parallel.

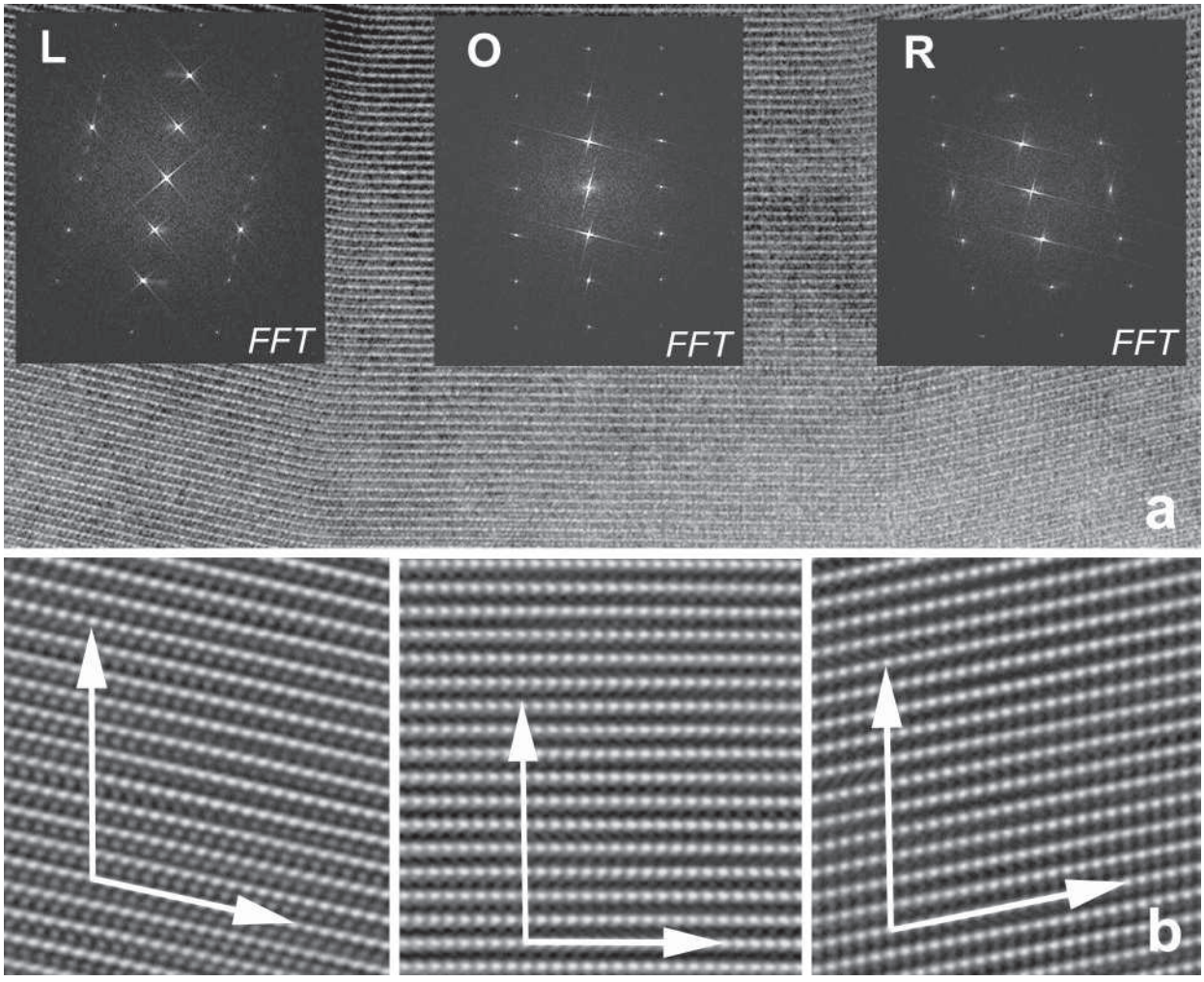

it leads to a two-layer unit cell (β = 97°), metrically equivalent to an **a**/3 shift between the first and third row. This projected 2D cell may be visualized as pairs of lizardite layers directly stacked one over the other with no translational component, but with adjacent pairs shifted by **a**/3.

[100] projections: HR images, Fourier-filtering, and SAED patterns

In contrast to the [010] diffraction patterns and images, the [100] diffraction patterns and images show variable ordered intrasector polytypes, as well as complex disordered sequences. The most important [100] feature is the concerted occurrence of specific stacking sequences from sector to sector (Dódony 1997a; Baronnet and Devouard 2005).

PS fibers with projected one-layer polytypes only are rare. Actually, fibers often show complex stacking, with locally ordered or disordered multilayer polytypes. The stacking sequences may vary from fiber to fiber, as well as within the single sector. In particular, ordered one- and two-layer sequences occur more frequently close to the fiber rim, whereas disordered sequences occur close to the core. Stacking faults, giving rise to intrafiber radial polytype variations, are conserved from sector to sector and form closed loops, similar to the ones in Figure 1b of Dódony (1997a), or in Figure 1 of Baronnet and Devouard (2005).

When the **a**/3 stacking component in the third dimension is taken into account, the actual periodicity may further increase. For example, the [100] projected one-layer polytype corresponds to a two-layer polytype.

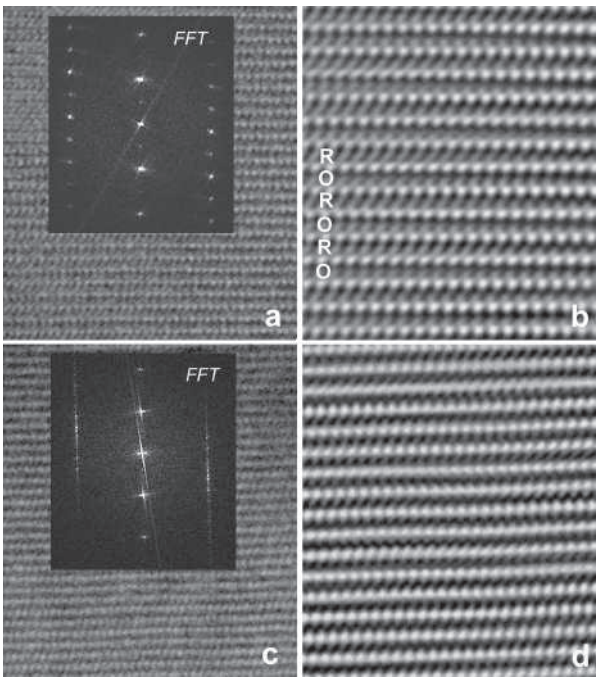

Figure 7. (**a**) and (**b**) Experimental and filtered [100] projected ordered two-layer polytypes, based on OR sequence (PS-30, S491); the FFT pattern (inset) shows evident 14 Å periodicity in the 02*l* rows; (**c**) and (**d**) experimental and filtered [100] projected disordered stacking sequence (PS-15, S1283); the FFT pattern (inset) shows highly streaked 02*l* rows.

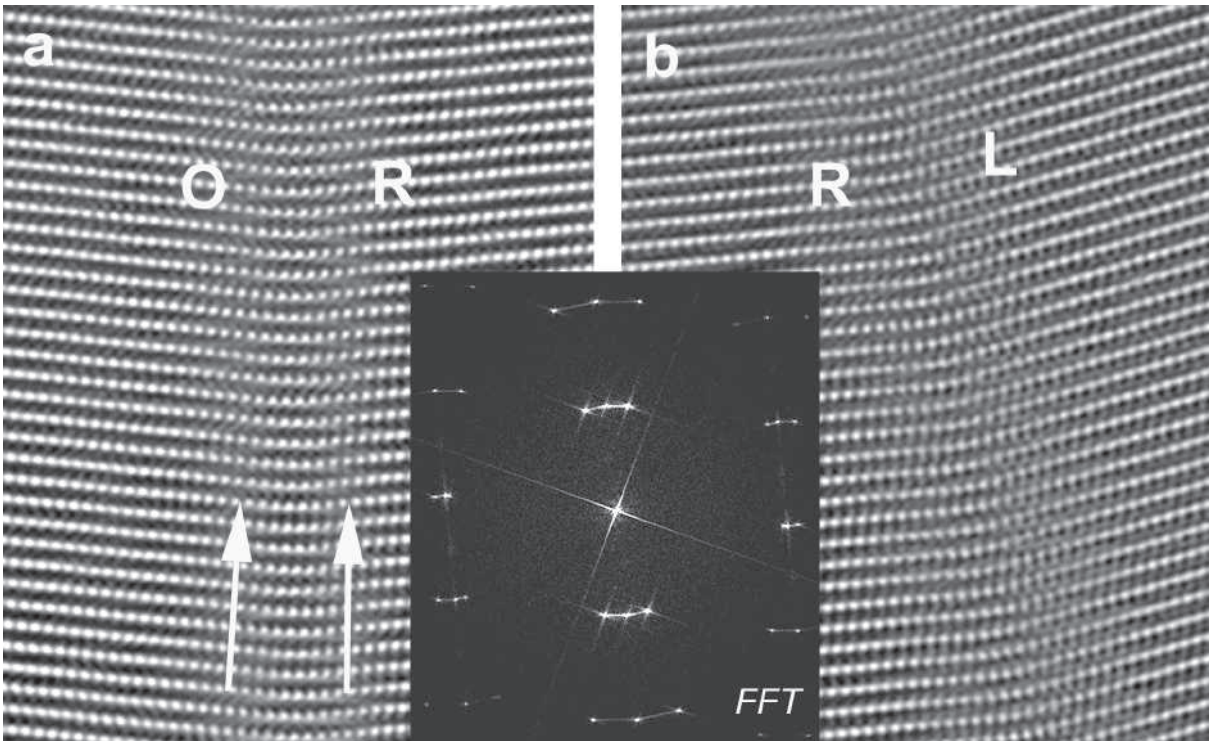

Figure 8. [100] Fourier-filtered images of the boundaries between adjacent sectors (**a**) O-R and (**b**) R-L in a PS-30 fiber (S491); part of the central R sector is not reported in the figure, due to size problems. 1:1 layers are continuous, with no tetrahedral-octahedral inversion. Broad contrast bands (arrows) run parallel to the sector boundary. The FFT (inset) was calculated sampling the three adjacent sectors. Note the streaked linear segments connecting adjacent 00*l* spots in the FFT.

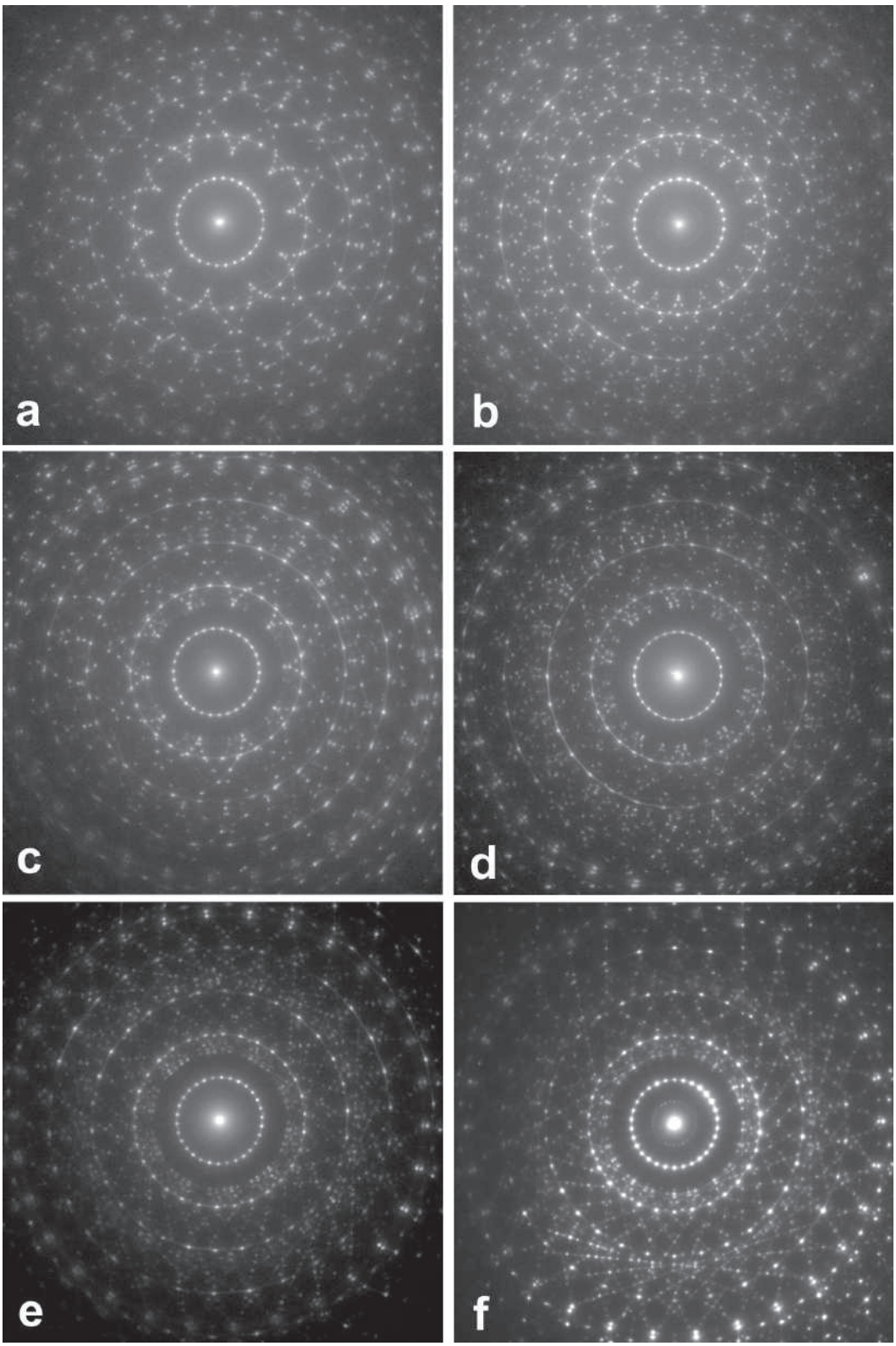

FIGURE 9. Experimental [100] SAED patterns of PS-30. (**a**) 10-cusps pattern of a projected one-layer PS fiber. (**b**) 20-cusps pattern of a projected two-layer PS fiber. (**c**) Pattern with 10 strong + 10 weak cusps. (**d**) Pattern with 20 + 10 cusps. (**e**) Pattern with 50 cusps (ten "groups" of five reflections). (**f**) Pattern with 60 cusps and evident diffraction chords.

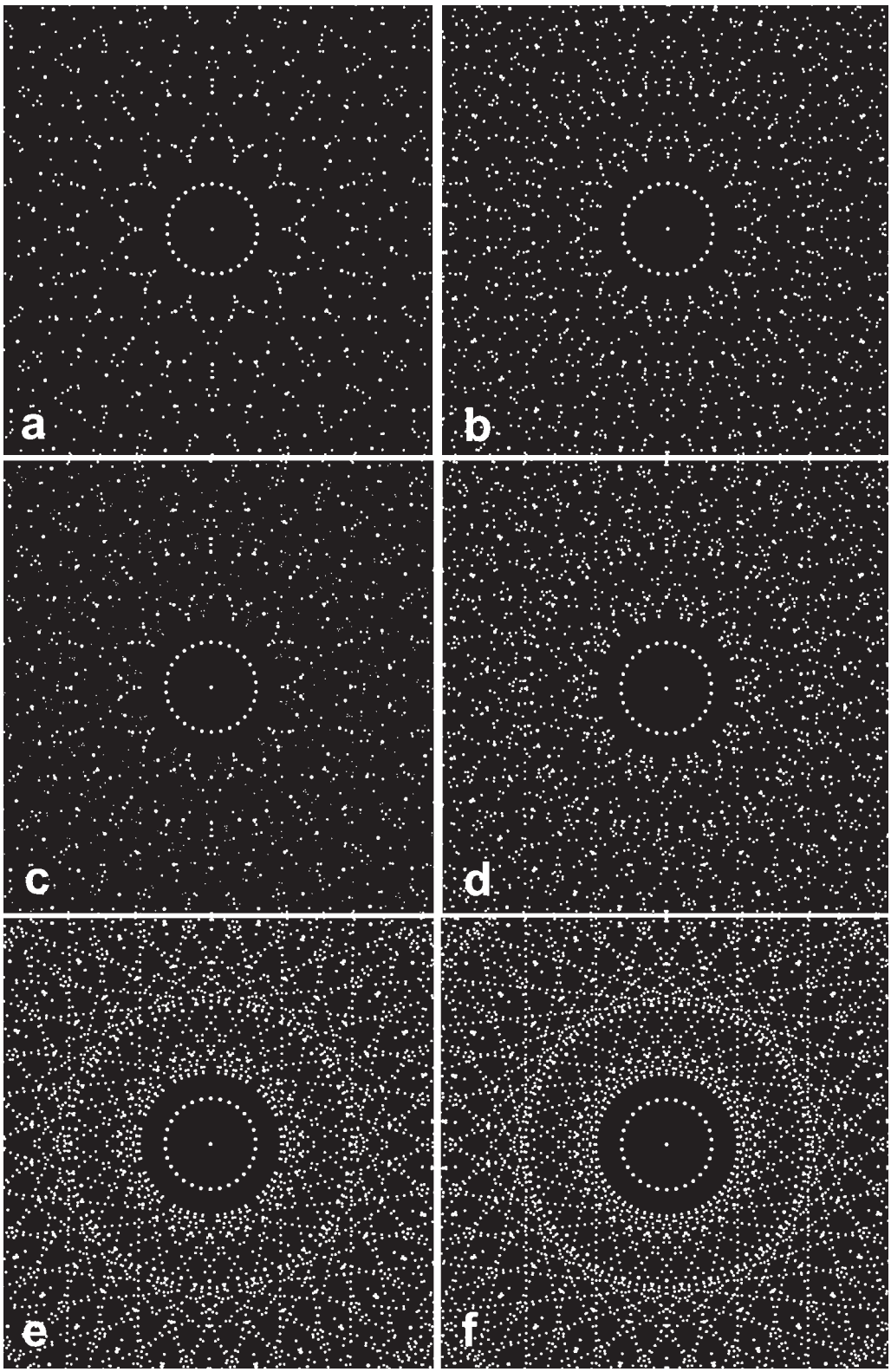

FIGURE 10. Simulated [100] SAED patterns. (**a**) "One-layer" polytypes and no intrasector stacking fault (10-cusps pattern). (**b**) "Two-layer" polytypes and no intrasector stacking fault (20-cusps pattern). (**c**) O + R sequences in the reference sector (10 + 10 cusps); the spots have been drawn with two different intensities to match the experimental pattern. (**d**) O + LO sequences in the reference sector (10 + 20 cusps). (**e**) O + LO + OR sequences in the reference sector (50-cusps pattern). (**f**) RL + LO + OR sequences in the reference sector (60-cusps pattern).

[100] projected one-layer polytypes and intersector polytype alternations. In agreement with Dódony (1997a) and Baronnet and Devouard (2005), we observe [100] projected one-layer polytypes with three different **c** stacking vectors within the same fiber. They produce three different 2D cells: an orthogonal cell (O) with b = 9.2 and c = 7.3 Å, a right-slanting (R) and a left-slanting (L) cell with b = 9.2, c = 7.4 Å, and α = 78° or 102°, respectively.

The stacking sequences are strictly controlled in adjacent sectors. In particular, they systematically follow regular counterclockwise O-R-L and O-L-R alternations, for projected one-layer PS-30 and PS-15, respectively. Figure 6 shows three adjacent sectors (L, O, and R, respectively) in a PS-30 fiber, together with the FFTs of each sector and the corresponding Fourier-filtered images. The FFTs (insets in Fig. 6a) show one-layer polytypes, without extra-reflections and streaking. The corresponding Fourier-filtered images (Fig. 6b) confirm ordered polytype sequences within each sector, with 102° left-slanting, orthogonal and 78° right-slanting **c** stacking vectors, respectively. Figure 6b shows that for triplets of adjacent L-O-R sectors, the three **c** vectors are parallel, whereas the **b** vectors are rotated by 12°.

[100] projected two-layer polytypes and intrasector disordered sequences. We found three different [100] ordered projected two-layer polytypes, based on stacking sequences RL (orthogonal 14 Å cell), LO (96° left-slanting 14 Å cell) and OR (84° right-slanting 14 Å cell). Figure 7a shows an example of ordered projected two-layer polytype in PS-30, based on OR stacking sequence. The corresponding FFT (inset) confirms two-layer polytypes, showing 02l and $0\bar{2}l$ diffraction rows with sharp 14 Å reflections. The Fourier-filtered image (Fig. 7b) shows ordered alternation of orthogonal stacking vectors (i.e., with no y shift) and oblique stacking vectors (angles of 78°, corresponding to y shift of **b**/6).

Figure 7c is an example of disordered stacking in PS-15. The FFT (inset) has sharp strong 7 Å reflections in 00l, with no streaking and extra-reflections; in contrast, 02l and $0\bar{2}l$ diffraction rows are heavily streaked. The Fourier-filtered image (Fig. 7d) shows a disordered sequence of orthogonal, 78° right-slanting and 102° left-slanting **c** stacking vectors. The basic alternation rules still hold (counterclockwise O-R-L and O-L-R alternations for PS-30 and PS-15, respectively). Therefore, in PS-30 the RL sequence transforms to LO in the nearest sector, and to OR in the next one; conversely, in PS-15 it transforms to OR first, and to LO later.

Sector boundaries. In PS-30 intersector boundaries are regular and sharp, with limited layer curvature, whereas in PS-15 they are wider and irregular, with extended curved layers. Figure 8 reports FFT and Fourier-filtered images of two adjacent O-R and R-L boundaries in PS-30; all three O, R, and L sectors have been selected for the FFT (inset), as evident from the three 00l rows, at 12° from one another. Special care was taken during filtering, to include the rectilinear streaks connecting the three 00l spots of adjacent O-R-L and corresponding to the curved portions at O-R and R-L sectors boundaries. Excluding the streaks from the filtering mask may simulate artifacts in the boundary structure. In both PS-15 and PS-30, our experimental (Fig. 6a) and Fourier-filtered images (Fig. 8) indicate continuous layers, with no tetrahedral inversion. Fourier-filtered images often reveal two transitional zones, extending for approximately 2–3 unit cells and appearing as broad contrast bands, parallel to the boundary plane (arrows in Fig. 8a).

The flexural nature of the sector boundaries has been previously analyzed by Baronnet and Devouard (2005). We agree with their interpretation, reformulated in terms of parallel or similar folds (Ramsay and Huber 1987). In parallel folds the thickness t measured orthogonally to the layer is constant. As a consequence, the reciprocal lattice streaks, connecting 00l spots

Table 1. Schematic unit cells of projected one-layer and two-layer polytypes

Projected polytype	Cell parameters					
	a	*b*	*c*	α	β	γ
O	5.3	9.2	14.7	90	97	90
R	5.3	9.2	15.0	78	97	90
L	5.3	9.2	15.0	102	97	90
RL	5.3	9.2	14.7	90	97	90
OR	5.3	9.2	14.8	84	97	90
LO	5.3	9.2	14.8	96	97	90

Table 2. Effects of intrasector radial stacking faults on cusp number and angular settings

Intrasector radial stacking faults		Stacking sequence in the reference sector	Number of cusps	Circular clockwise settings of the cusps (020 spots)*					
				0°	6°	12°	18°	24°	30°
No intrasector radial stacking fault									
1	One "one-layer" sequence	O	10	x					
2	One "two-layer" sequence	RL	20	x			x		
One intrasector radial stacking fault									
3	Two "one-layer" sequences	O+R ≡ O+L	20	x		x			
4	One "one-layer" sequence plus one "two-layer" sequence	O+RL†	20	x			x		
5	" "	O+OR	30	x	x			x	
6	" "	O+LO	30	x		x			x
7	Two "two-layer" sequences	RL+LO ≡ RL+OR	40	x	x		x	x	
Two intrasector radial stacking faults									
8	Three "one-layer" sequences	O+R+L	30	x		x		x	
9	Two "one-layer" sequences plus one "two-layer" sequence	L+LO+O	40	x		x		x	x
10	One "one-layer" sequence plus two "two-layer" sequences‡	O+LO+OR	50	x	x	x		x	x
11	Three "two-layer" sequences‡	RL+LO+OR	60	x	x	x	x	x	x

* Starting from any 020 spot of O or RL polytype and periodically repeated every 36°.
† The sequence O+RL matches RL.
‡ Wings become not clearly distinguishable and only cusps are recognized. 02l chords are progressively more evident.

from adjacent sectors, should be arc-shaped. On the contrary, similar folds show identical bounding surfaces, with constant thickness *T*, measured anywhere in the fold but parallel to the axial surface. In this model, the thickness *t* is maximal at the fold axis and minimal along the flanks. In polygonal structures with intersector curve portions, *t* increases up to

$$t = \frac{d_{00l}}{\cos(\varphi/2)}$$

at the fold hinge, where d_{00l} is the interplanar distance of flat layers and φ the angle subtending a polygonal sector (12° in PS-30 and 24° in PS-15). Therefore, similar folds differ from parallel folds in that they introduce variable, decreasing reciprocal lattice vectors. Namely, the streaks connecting 00*l* spots will be linear segments rather than arcs. As pointed out by Baronnet and Devouard (2005) and further detailed here (see, for instance, the FFT in Fig. 8), both FFTs and SAED patterns actually show rectilinear streaks in 00*l* pseudo-rings, suggesting that sector boundaries in PS are equivalent to similar folds. The variable interplanar spacings in flat- and curved-layer regions of PS may perhaps explain the 00*l* peak asymmetry (deconvolved into one 7.2 and one 7.3 Å component) observed by Cressey et al. (1994) in the synchrotron XRPD patterns of polygonal serpentine.

Experimental [100] SAED patterns. All the [100] SAED patterns are highly symmetrical, due to the manifold repetition of the given reciprocal lattices. They are characterized by 00*l* rings, each constantly consisting of 30 reflections, and by variable numbers of wings and cusps, i.e., the points connecting two adjacent wings (Fig. 9).

Although PS-30 and PS-15 produce similar patterns, they are distinguishable from one another based on subtle diffraction details. First, PS-15 has alternating weak and strong reflections distributed around the 7 Å ring, whereas PS-30 has equivalent intensities. This lowered symmetry is usually accompanied by inward and outward shifts of alternating spots during diffraction focusing. Following the dynamic calculations by Dódony (1997a), we explain this lowered symmetry as due to major deviations from the Friedel law, due to the strongly polar structure of the 1:1 lizardite layer. In fact, whereas 00*l* and 00$\bar{l}$ do not overlap in PS-15, they do overlap and merge in PS-30. Second, the rectilinear streaks linking 00*l* spots of adjacent sectors are arranged as a 30-sided polygon in PS-30, and as two interlocked 15-sided polygons, rotated by 12°, in PS-15.

The simplest [100] SAED patterns correspond to PS fibers with only "one-layer" ordered sequences (with counterclockwise O-R-L and O-L-R alternations in PS-30 and PS-15, respectively). They consist of 10 cusps, each separated by 36° (Fig. 9a). PS fibers with "two-layer" ordered sequences (counterclockwise OR-RL-LO and OR-LO-RL alternations in PS-30 and PS-15, respectively), produce [100] SAED patterns with 20 cusps, each separated by 18° (Fig. 9b).

Nevertheless, PS SAED patterns may be more complex, with larger numbers of cusps and diffraction chords (Figs. 9c to 9f). Figure 9c shows ten intense cusps, plus another set of ten less intense cusps; Figure 9d shows 30 cusps (20 + 10), all with similar intensities, whereas Figures 9e and 9f correspond to more complex cases, with 50 and 60 cusps, respectively, and visible diffraction chords. Both HR images and SAED simulations (see later) indicate that these patterns are due to the occurrence of intrasector radial stacking faults (i.e., they correspond to PS fibers with different "one-layer" and/or "two-layer" sequences within the same sector).

Simulated SAED patterns for ordered and faulted sectors. Simulation of SAED patterns was done by Dódony (1997a) and Baronnet and Devouard (2005), who calculated the FFT of direct space models. Furthermore, Dódony (1997a) reported [100] reciprocal lattice sections built up by appropriate propagation of 15 and 30 reciprocal lattices, one for each sector, and used them to deny the validity of the two PS structure models previously proposed by Chisholm (1992) and by Baronnet et al. (1994). Actually, the reproduction of the complex [100] SAED patterns is an effective way for the validation of any structural hypothesis, allowing a quick selection of models worthy of further testing.

Therefore, we calculated the SAED patterns using an ad-hoc FORTRAN program, capable of generating the reciprocal coordinates for any polytype sequence. The computer code calculates the reciprocal lattice in a given sector and, by application of the assumed stacking operators, it produces the three adjacent sectors. Taking into account the rotation angle of 12° or 24° between adjacent sectors, the code combines the three reciprocal lattices and projects them along any chosen direction. Finally, by propagation of the three sectors through the appropriate rotation matrix, it calculates the diffraction pattern of the whole fiber.

The lattice parameters used for the simulations are summarized in Table 1, for the polytypes O, R, L, RL, OR, and LO. In PS-30, the angle between the **b** vectors of adjacent sectors is 12°; the counterclockwise alternation of polytypes is O-R-L and OR-RL-LO for one- and two-layer structures, respectively. In PS-15, the angle between **b** vectors of adjacent sectors is 24°; the counterclockwise alternation of polytypes is O-L-R and OR-LO-RL for one- and two-layer structures, respectively. The **a** vectors of all polytypes point along the fiber axis, causing the simultaneous diffraction of all the sectors when the fiber is properly aligned. As our simulations do not carry any information about spot intensities, the simulated PS-15 and PS-30 patterns are indistinguishable.

First, we have reproduced the basic 10- and 20-cusps experimental patterns (Table 2, rows 1 and 2, respectively), confirming the O-R-L and O-L-R counterclockwise polytype alternation of PS-30 and PS-15, respectively. Figures 10a and 10b show the simulated [100] SAED patterns for comparison with the experimental ones (Figs. 9a and 9b). Simulated [100] patterns with deliberately inverted counterclockwise alternations (e.g., O-L-R for projected one-layer polytype PS-30) do not match the experimental ones.

Simulated patterns allow easy indexing of the experimental patterns (as shown in Figs. 11a and 11b). As previously stressed, rings are composed of 00*l* spots. The first crown of wings is composed of 02*l* spots of different sectors, with each cusp corresponding to 020 spots.

We also used our program to calculate the effects induced by one or two radial stacking faults and found nine more possible [100] SAED patterns (Table 2, rows 3–11, valid for both PS-15 and PS-30). Further stacking faults would not introduce any more diffraction spots. Simulations explain all the observed patterns, as evident by comparing Figures 9c–9f and Figures 10c–10f. All

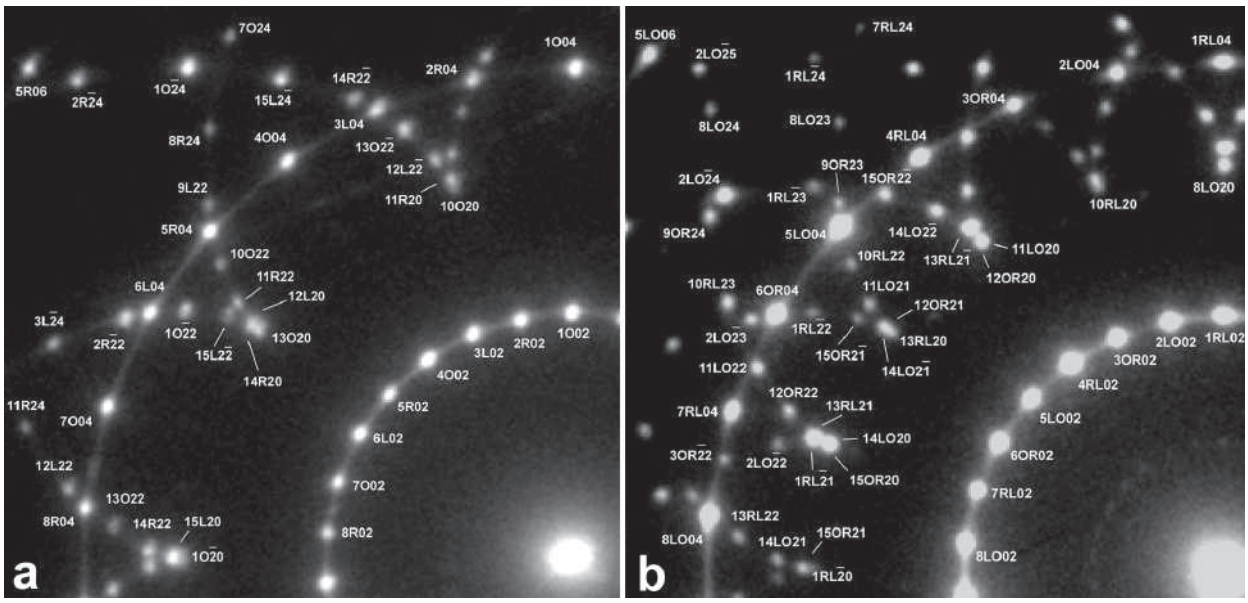

FIGURE 11. (**a**) and (**b**) Indexed [100] experimental SAED patterns (10- and 20-cusps, respectively). The first number corresponds to the sector number producing the spot (counting counterclockwise from an O or RL sector, as in Figure 10a by Baronnet and Devouard 2005). Letters correspond to the polytype stacking (O, R, L, RL, OR, and LO). The last two numbers are the *k* and *l* indices of the spot.

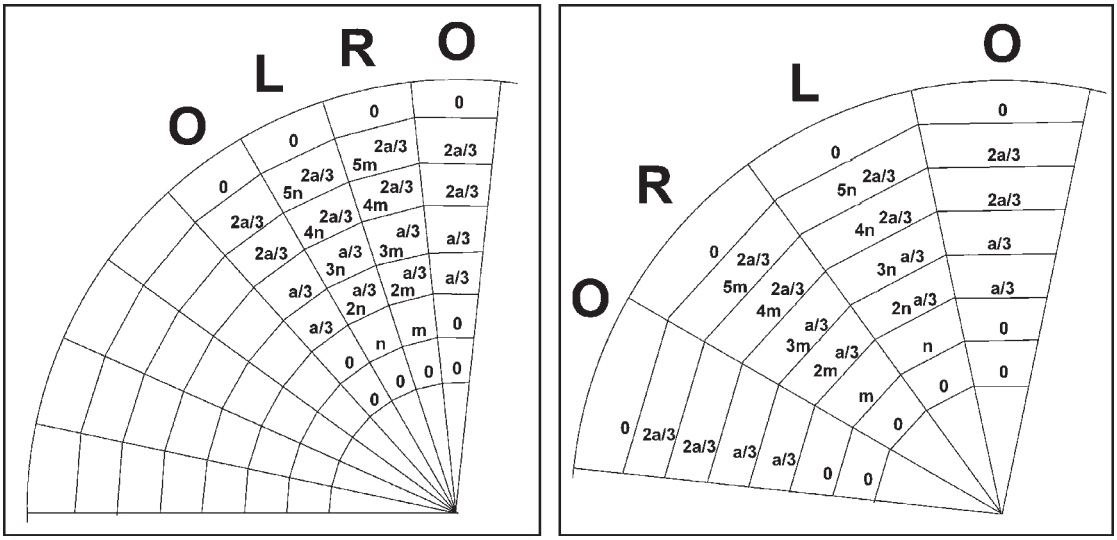

FIGURE 12. (**a**) and (**b**) 1:1 layer sequences in PS-30 and PS-15. The coordinates refer to a starting layer assumed as origin (0). *m* and *n* stand for the decomposition of a **b**/3 shift oblique to the fiber axis. *m* is equal to **a**/2 – **b**/6 and *n* is equal to **a**/2 + **b**/6. Based on convention, +**b** points counterclockwise.

the spots of these complex patterns can be explained as a combination of the two previous simple patterns (10- and 20-cusps patterns), with the appropriate mutual rotations. Therefore, the number and position of cusps depend on the faulted polytype sequences. In contrast, the 00*l* rings show constant features regardless of what polytypes are present in the fiber.

In particular, two different "one-layer" sequences (i.e., O + R or O + L) may coexist within the same sector (Table 2, row 3). The corresponding simulated [100] pattern (Fig. 10c) has 20 cusps, at 0, 12, 36° and so on (clockwise values starting from any reference cusp), matching the experimental pattern shown in Figure 9c.

PS fibers with one radial stacking fault, connecting "one-layer" and "two-layer" sequences, give [100] SAED patterns with 30 cusps, at 0, 6, 24, 36° (O + OR; row 5), or at 0, 12, 30, 36° (O + LO; row 6). Note that O + RL (row 4) matches the ordered "two-layer" RL polytype, showing 20 cusps separated by 18°. The experimental pattern of Figure 9d fits the simulation of Figure 10d, thus corresponding to O + LO. The number of cusps increases to 40 when sectors host two "two-layer" sequences (i.e., RL + LO or RL + OR), with cusps at 0, 6, 18, 24, 36° (row 7).

TABLE 3. Indexed XRPD pattern of PS-30 (S491)

d_{obs}	I/I_0	O	L	R
7.338	100	0 0 2	0 0 2	0 0 2
4.613	6	0 2 0	1 1 1	1 1 1
4.586	6	1 1 0	1 1 0	1 1 0
4.536	5	1 1 1	0 2 0	0 2 0
4.415	4		1 1 1	1 1 1
4.264	3	1 1 1	1 1 2	1 1 2
4.094	3	1 1 2	1 1 1	1 1 1
3.908	2	0 2 2	1 1 2	1 1 2
3.661	59	0 0 4	0 0 4	0 0 4
3.529	2	1 1 3	0 2 2	0 2 2
3.360	2		1 1 3	1 1 3
3.182	1	1 1 3	0 2 4	0 2 4
3.021	1	1 1 4	1 1 3	1 1 3
2.866	1	0 2 4	1 1 4	1 1 4
2.729	1	1 1 4	1 1 5	1 1 5
2.661	2	1 3 0	1 3 1	1 3 1
2.590	5	1 3 1	1 3 2	1 3 2
2.550	5	1 3 2	1 3 1	1 3 1
2.455	19	1 3 2	1 3 1	1 3 1
2.279	3	1 3 3	1 3 2	1 3 2
2.217	2	1 3 4	1 3 3	1 3 3
2.158	1	0 2 6	1 1 6	1 1 6
2.093	5	1 3 4	1 3 3	1 3 3
2.088	4	_	2 2 3	2 2 3
2.030	1	1 3 5	1 3 4	1 3 4
1.912	1	1 3 5	1 3 6	1 3 6
1.855	1	1 3 6	1 3 5	1 3 5
1.829	1	0 0 8	0 0 8	0 0 8
1.747	4	1 3 6	3 1 0	3 1 0
1.598	1	1 3 7	1 5 5	1 5 5
1.551	4	2 4 5	2 2 7	2 2 7
1.538	10	0 6 0	0 6 2	0 6 2
1.505	3	0 6 2	0 6 0	0 6 0
1.463	2	0 0 10	0 0 10	0 0 10
1.424	1	1 3 9	3 3 6	3 3 6
1.416	1	0 6 4	0 6 2	0 6 2

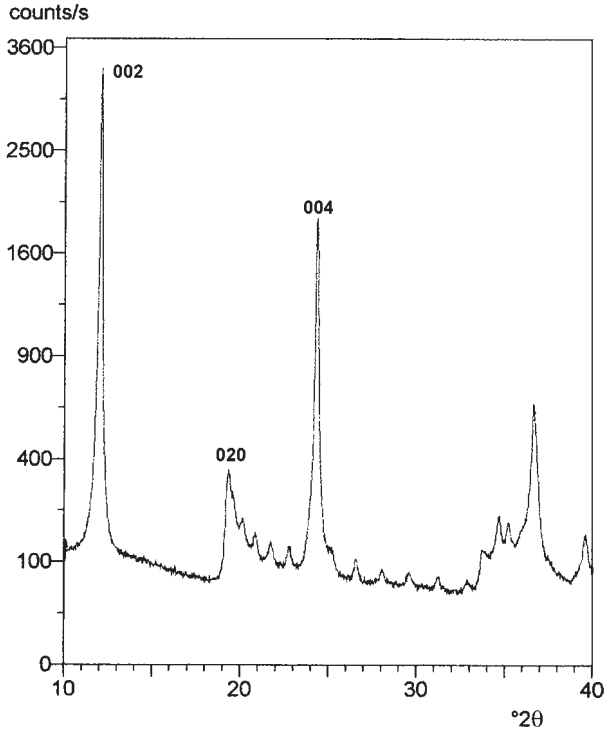

FIGURE 13. X-ray powder diffraction pattern of PS-30 (S491).

Four different patterns are possible for sequences with two intrasector radial stacking faults (rows 8–11). Triple "one-layer" sequences O + R + L result in SAED patterns with 30 cusps separated by 12°, i.e. at 0, 12, 24, 36°. The number of cusps increases to 40 in L + LO + O, with cusps clustered as a sequence of triplets and a single cusp. Finally, O + LO + OR (row 10) produces 50 cusps, organized as clusters of five cusps (Figs. 9e and 10e).

The most complex case is represented by three different "two-layer" polytypes in the same sector, RL + LO + OR (row 11), producing 60 cusps, each separated by 6° (Figs. 9f and 10f). In the last cases, wings are no longer evident and only the cusps may be recognized. However, the patterns now become characterized by 02*l* diffraction "chords."

Using the SAED geometry only, the determination of which polytype is in the core and which is in the outer fiber seems difficult. A possible hint comes from the detailed analysis of the shape of the diffraction spots; for instance, we expect less **b** translations in the inner sectors, producing broader spots in the **b*** direction.

Origin of diffraction "chords." The most evident diffraction chords correspond to 02*l* diffraction rows that originate due to the close lattice coincidence within the individual polytypically faulted sectors. Actually, a sector consisting of O + R + L stacking sequences has common **b** and variable **c** directions. In the reciprocal lattice, this means variable **b*** direction and just one common **c*** direction (namely $\mathbf{c}_O^* // \mathbf{c}_R^* // \mathbf{c}_L^*$). Moreover, because **b**, and d_{02l}^*, are equal for the three polytypes, all the 02*l* spots lay along a common line.

As the α* angle in R or L deviates from 90° by an angle defined by

$$\varphi = \pm\tan^{-1}[\mathbf{c}_O^*/(3\ \mathbf{b}_O^*)],$$

the 020 spot will shift by

$$\Delta z^* = \pm 2\ \mathbf{b}_O^* \tan\varphi = 2\ \mathbf{b}_O^*\ (\mathbf{c}_O^*/3\ \mathbf{b}_O^*) = \pm 2/3\ \mathbf{c}_O^*.$$

Namely, radial stacking faults introduce additional 02*l* spots, shifted by 2/3 $\mathbf{c}_O^*$.

Similarly, intrasector polytype faults within a two-layer sequence introduces new spots, spaced by 1/3 $\mathbf{c}_O^*$ and aligned along an evident diffraction "chord." Finally, the rotational symmetry of polygonal serpentine introduces a total of 30 chords. Other 0*kl* structures similar to 02*l* chords appear in the SAED and can be derived by the same mechanism.

3D polytype assemblages, octahedral rotations and cyclic twins

The actual polytype sequence within any given PS sector may be identified based upon the [100] and [010] projections. In the simplest cases, [100] show projected one-layer sequences, whereas [010] always show two-layer periodicities. Therefore, we may use the comprehensive tabulation of the possible two-layer lizardite polytypes of Dódony (1997b) to identify the polytype sequences corresponding to the observed unit cells reported in Table 1. In particular, the unit cell of the projected O polytype matches the M5 polytype of Dódony (1997b) (by transforming his acute setting with β = 83° into our obtuse

setting with $\beta = 97°$). Conversely, the unit cells of the R and L polytypes match both the M15 and M16 polytypes of Dódony (1997b), after transformation of his setting into the current one by 120° rotation.

PS consists of M5 polytypes (O sector) surrounded by two M15 (or M16) polytypes (adjacent R and L sectors). Whereas M5 requires 1:1 layers with common octahedral orientations (e.g., positively slanting octahedra), both M15 and M16 have two different octahedral orientations, as required by the 60° rotation present in the stacking operations (Dódony 1997b).

Each 1:1 polygonalized layer would consist of a regular, continuous tetrahedral sheet, overlapping a continuous octahedral sheet that shifts the octahedral distribution, from positive to negative. This inversion is geometrically described by a 60° rotation perpendicular to the layer, namely as a symmetry operation of the ideal tetrahedral sheet that becomes a pseudosymmetry operation in the trigonal octahedral sheet. In conclusion, the PS arrangement may be described as a cyclic fivefold lizardite pseudo-twin, producing local, non-crystallographic fivefold symmetries for both PS-15 and PS-30. The overall arrangement is sketched in Figure 12, for both PS-15 and PS-30. The pattern shows the interlayer relationships in terms of the lattice parameter **a** and of the operations *m* and *n*, equivalent to $\mathbf{a}/2 - \mathbf{b}/6$ and $\mathbf{a}/2 + \mathbf{b}/6$, respectively. These two operations represent the decomposition of a **b**/3 shift oblique to the fiber axis.

Apparently, octahedral rotation seems the only way to explain the M5 and M15 (or M16) coexistence. Hypothetically, octahedral rotation might be directly proved by [001] data, such as images or electron diffraction data discriminating the two octahedral orientations in adjacent sectors.

Finally, M15 and M16 might be distinguished based upon [010] diffractions (see Dódony 1997b, for a comparison of the different symmetries). Up to now, we do not have reliable data to discriminate between the two possibilities.

XRPD additional reflections

The characteristic features of the PS X-ray powder diffraction patterns are clusters of additional satellite reflections (Fig. 13 and Table 3; S491). One cluster occurs on the high-angle side of the peak at $d = 4.613$ Å (d_{020} in the *C*-centered unit cell). The other one occurs on the high-angle side of the peak at $d = 3.661$ Å (d_{004}). These clusters may be more or less evident, depending upon PS crystallinity and abundance. In particular, the clusters become more evident along the sequence S1283, S265, S1279, S491.

Similar additional reflections have been reported for polygonal serpentine (e.g., Morandi and Felice 1979; Varlakov 1984; Logar 1992) and interpreted as due to multilayer polytypes (see the case of the Unst-type serpentine, firstly interpreted as multilayer lizardite but later demonstrated to be polygonal serpentine; Papp 1990).

We tried to index the satellites and used them for the unit-cell parameter refinement. Using the M5 polytype only (starting values of $a = 5.3$, $b = 9.2$, $c = 14.7$ Å, $\beta = 97°$), we obtained the refined values of $a = 5.343(1)$, $b = 9.227(10)$, $c = 14.74(2)$ Å, $\beta = 96.93(3)°$. This solution is oversimplified, because it was obtained using only the O sectors, namely the ones that show a one-layer orthogonal cell in [100] projections. It results in partial indexing of the pattern; in particular, reflections at $d = 4.415$ and $d = 3.360$ Å are not indexed (Table 3). Conversely, by introducing the R or L sectors with possible M15 or M16 polytypes, we obtained the refined values of $a = 5.351(1)$, $b = 9.225(14)$, $c = 15.06(3)$ Å, $\alpha = 78.16(4)$ or $101.84(4)$, $\beta = 96.89(5)$, $\gamma = 89.92(7)°$, and all the reflections are indexed (Table 3).

In conclusion, our calculations demonstrate that the satellites arise from polytype effects. Namely, the modification of the polytype from one sector to the adjacent one introduces new interplanar spacings that are responsible for the new reflections. However, in our experience the distribution of satellite reflections does not show any obvious, robust-resistant XRPD fine structure, leading to the different polytype sequences. This feature may constitute quite a challenge for future Rietveld refinements, although the sharp differences in the powder diffraction patterns revealed by the calculations of Dódony (1997b) for M5, M15, and M16 are a helpful feature.

Discussion and concluding remarks

3D analysis of polytypism

The 3D study sheds new lights on polytypism in PS. In particular, even the simplest sequences observed in [100] projections are based upon two-layer sequences, as revealed by the [010] projection. Based upon the observed electron diffraction patterns and high-resolution images, we derive alternating M5 and M15 (or M16) polytypes among adjacent sectors. Most importantly, the M15 and M16 polytype stacking sequences contain 60° rotations that change the octahedral distribution.

The mineralogical relevance of polygonal serpentine

Owing to the difficulties in identifying the serpentine minerals, polygonal serpentine has been neglected before the advent of TEM as a routine tool for mineral investigation. Actually, several low-grade occurrences are known, as shown by Mellini (1986), Dódony (1997a), and Baronnet and Devouard (2005). Although the mineral also is present in mesh cores and bastites (Cressey and Zussman 1976; Cressey 1979; Viti and Mellini 1998), as well as in kimberlitic segregations (Podvysotskiy 1985; Mitchell and Putnis 1988), the most typical occurrence is in massive serpentine veins cutting serpentinites, such as the ones described here.

We wonder how many studies may be partially biased by neglecting PS. For instance, PS has been wrongly identified as multi-layer lizardite (e.g., the case of the Unst-type serpentine) and its intrinsic rotational disorder features have been wrongly attributed to non-polygonal lizardite, as already remarked by Papp (1990). The problem is not merely one of mineral nomenclature or mineral identification. For instance, the correct recognition of PS is fundamental during the experimental or field determination of the serpentine stability; here, PS should not be confused with chrysotile, just because it appears to be a non-lamellar, fibrous serpentine or because it produces X-ray patterns characteristic of disordered structures.

The problem also occurs during asbestos hazard assessment, and even during *post-mortem* damage evaluation; namely, we wonder whether PS should be classified with fibrous chrysotile, or with non-fibrous lizardite, even as far as economic, labor, and environment legislation is concerned.

Structure models: continuous vs. inverted layers

Since the pioneering work of Middleton and Whittaker (1976), the structure model of polygonal serpentine has improved through the years. Most of the work has been done using electron diffraction and electron microscopy. Nowadays, the structural principles seem established, for both PS-15 and PS-30. However, some debate on the 1:1 layer polarity still persists. Baronnet and Devouard (2005) confirmed the simplest model based upon a common polarity throughout the whole polygonal loop. Conversely, Dódony and Buseck (2004) supported the model of Dódony (1997a), requiring tetrahedral inversion at the sector boundaries.

In our experience, properly aligned PS-15 and PS-30 (such those ones producing the patterns in Fig. 9) always show continuous layers, with no inversion. Examples may be found in several images, such as Figures 6 or 8. However, images with apparent inversion (generated as an artifact) are possible; for instance, apparent offsets arise after suppression, during image treatment, of the diffuse streaks between adjacent 00*l* spots. When suggesting tetrahedral inversion, Dodony (1997a) claimed that "reciprocal lattices construction on the basis of the PS models of Baronnet et al. (1994)...do not match the SAED pattern in Fig. 1a" (p. 40). However we notice that Figure 1a in Dódony (1997a) is an experimental 10-cusps [100] SAED pattern of projected one-layer polytype, apparently compared to a 20-cusps diffraction pattern calculated from the model of Baronnet et al. (1994) for projected two-layer sequences. Finally, the Dódony's model cannot be reconciled with fibers consisting of 15 sectors because this would present an odd number of polarity reversals (Baronnet and Devouard 2005). Therefore, both the current data and the comparison with pre-existing interpretations confirm the presence of continuous 1:1 layers in polygonal serpentine with no tetrahedral inversions.

Growth mechanism

The study of complex balangeroite-chrysotile-polygonal serpentine veins showed progressive substitution along that series (Mellini 1986). In particular, the structural and textural arrangements were consistent with transformation from small chrysotile fibers to large polygonal serpentine, according to a growth pattern from the core to the rim. The point was strengthened by Grauby et al. (1998), who experimentally demonstrated that polygonal serpentine may form from chrysotile fibers with 50–100 nm diameter. Finally, Baronnet and Devouard (2005) proposed solid-state polygonalization of the chrysotile cylinder, followed by both limited inner growth and unlimited outer overgrowth.

In the present case, the data suggest that PS forms by replacement of ctl fibers + poorly crystalline material. Smaller polygonalized fibers (100–300 nm in diameter) represent an intermediate structure between ctl and PS. The growth mechanism may be locally complex and irregular, typically producing "telescope" (such the ones observed by Mitchell and Putnis 1988) or indented "saw-teeth" shapes (such the ones of Fig. 3), surrounding a compact central core. The latter case may be described as overgrowth on ctl fiber bundles (possibly consisting of one or several ctl fibers), with subsequent polygonalization. The outer (001) faces contain the fast-growing directions of serpentine and develop easily, until they come in contact with geometrical unconformities represented by misaligned ctl fibers that locally interrupt the PS development. These misaligned fibers are overgrown, and eventually become embedded within the saw-teeth PS fiber.

Although deformation does not seem necessary to promote the chrysotile-to-polygonal serpentine transformation (as demonstrated by the stress-free hydrothermal experiments of Grauby et al. 1998), deformation was present at least in the cases of samples S491 and S265, but apparently it acted only to induce the parallel orientation of the outer PS fibers. In fact, this outer shearing stress affects the gliding surface by orienting the fibers such that there is limited propagation of inward stress.

In our opinion, the ctl-to-PS transformation is an Ostwald ripening process, with the first-formed, kinetically favored phase (the cylindrically curled-layer ctl), progressively replaced by the ripened, energetically favored form (the flat-layer serpentine). Normally, the latter would be regular lizardite. However, in the present case the existing ctl fibers act as heterogeneous nucleation centers for lizardite, that are fitted to the circular shape by polygonalization. The need to fit a curled substrate eventually results into a shape that might be defined as a cyclical, polysynthetic twin.

Why PS-15 or PS-30?

The general principles governing the PS-15 and PS-30 structures are the same, differing only in the amount of shearing from one sector to the next (**b**/3 vs. **b**/6) and, obviously, in the number of sectors. At least in our specimens, the two forms seem to occur separately from vein to vein, with one dominant over the other. However, PS-30 is the most common form. Furthermore, PS-15 is usually less developed and more defective than PS-30. Therefore, we may expect that the two forms differ energetically. As remarked by Baronnet et al. (1994), this difference is derived from the different elastic interactions between the radial dislocation walls. Assuming that the energy E_{PS} stored within each is dependent upon B^2, where $\boldsymbol{B}$ is the Burgers vector of the dislocation, we obtain rough estimates of $E_{PS\text{-}15} = 15 \times 1^2 = 15$, vs. $E_{PS\text{-}30} = 30 \times (1/2)^2 = 7.5$ (arbitrary units). Namely, the elastic energy stored within the sector boundaries of PS-15 would be twice the energy stored within the sector boundaries of PS-30. In conclusion, we expect that PS-30 is energetically favored over the less stable PS-15. This difference would be more important when surface effects dominate over volume effects (namely, close to the PS core, where PS receives the structural imprint that is later conserved during the outward growth). This energy difference may be related to the interplanar d_{00l} spacings, which are significantly greater in PS-15 than in PS-30 (from d_{00l} = 7.38 Å to d_{00l} = 7.22 Å, or 14.76 and 14.44 Å for the two-layer polytypes, respectively).

Acknowledgments

This study was started during a TEMPUS stage of M.L. in Siena. We are grateful to Istvan Dódony and Fred Wicks for the careful reviews.

References cited

Baronnet, A. and Devouard, B. (1996) Topology and crystal growth of natural chrysotile and polygonal serpentine. Journal of Crystal Growth, 166, 952–960.

——— (2005) Microstructures of common polygonal serpentines from axial HRTEM imaging, electron diffraction, and lattice-simulation data. Canadian Mineralogist, 43, 513–542.

Baronnet, A. and Mellini, M. (1992) Polygonized serpentine as the first mineral with five-fold symmetry. Abstracts of the 29th International Geological Congress (Tokyo), 3, 682.

Baronnet, A., Mellini, M., and Devouard, B. (1994) Sectors of polygonal serpentine. A model based on dislocations. Physics and Chemistry of Minerals, 21, 330–343.

Chisholm, J.E. (1992) The number of sectors in polygonal serpentine. Canadian Mineralogist, 30, 355–365.

Cressey, B.A. (1979) Electron microscopy of serpentinite textures. Canadian Mineralogist, 17, 741–756.

Cressey, B.A. and Zussman, J. (1976) Electron microscopic studies of serpentinites. Canadian Mineralogist, 14, 307–313.

Cressey, B.A., Cressey, G., and Cernik, R.J. (1994) Structural variations in chrysotile asbestos fibers revealed by synchrotron X-ray diffraction and high-resolution transmission electron microscopy. Canadian Mineralogist, 32, 257–270.

Dódony, I. (1997a) Structure of the 30-sectored polygonal serpentine. A model based on TEM and SAED studies. Physics and Chemistry of Minerals, 24, 39–49.

——— (1997b) Theoretical derivation and identification of possible two-layer lizardite polytypes. In S. Merlino, Ed., Modular Aspects of Minerals, 1, p. 57–80. EMU Notes in Mineralogy, Eötvös University Press, Budapest.

Dódony, I. and Buseck, P.R. (2004) Serpentine close-up and intimate: an HRTEM view. International Geology Review, 46, 507–527.

Eckhardt, F.J. (1956) Röntgenographische untersuchungen am schweizerit. Neues Jahrbuch Mineralogie Monatshefte, 32–43.

Grauby, O., Baronnet, A., Devouard, B., Schumaker, K., and Demirdjian, L. (1998) The chrysotile-polygonal serpentine-lizardite suite synthesized from a 3 MgO-2SiO_2-excess H_2O gel. Abstracts of European Mineralogy Petrology Geochemistry (EMPG VII). Terra Nova Supplement, 10, 24.

Jiang, S. and Liu, W. (1984) Discovery and its significance of Povlen-type hydrochrysotile. Acta Geologica Sinica, 58, 136–142 (in Chinese).

Krstanović, I. (1967) X-ray study of six-layer ortho-serpentine. American Mineralogist, 52, 871–876.

——— (1997) Serpentine mineral from Crni Kamen, Serbia. Neues Jahrbuch Mineralogie Monatshefte, 451–465.

Krstanović, I. and Pavlović, S. (1964) X-ray study of chrysotile. American Mineralogist, 49, 1769–1771.

Logar, M. (1992) Polygonal serpentine from Kačanik area. Annales Geologica Peninsula Balkanica, 56, 329–344.

Logar, M. and Viti, C. (1996). Transmission electron microscopic studies of polygonal serpentine from Kačanik (Serbia, Yugoslavia). Abstracts IV Conference of the Serbian Crystallographic Society, 34.

Mellini, M. (1986) Chrysotile and polygonal serpentine from the Balangero serpentinite. Mineralogical Magazine, 50, 301–306.

Middleton, A.P. and Whittaker, E.J.W. (1976) The structure of Povlen-type chrysotile. Mineralogical Magazine, 14, 301–306.

Mitchell, R.H. and Putnis, A. (1988) Polygonal serpentine in segregation-textured kimberlite. Canadian Mineralogist, 26, 991–997.

Morandi, N. and Felice, G. (1979) Serpentine minerals from veins in serpentinite rocks. Mineralogical Magazine, 43, 135–140.

Papp, G. (1990) A review of multi-layer lizardite. Annales Historico-Naturales Musei Nationalis Hungarici, 82, 9–17.

Podvysotskiy, V.T. (1985) Serpentine-carbonate mineralization in kimberlites. International Geology Review, 27, 810–823.

Ramsay, J.G. and Huber M.I. (1987) The techniques of modern structural geology, folds and fractures, 2, p. 347–351. Academic Press Inc., London.

Rumori, C., Mellini M., and Viti, C. (2004) Oriented, non-topotactic olivine → serpentine replacement in mesh-textured, serpentinized peridotites. European Journal of Mineralogy, 16, 731–741.

Varlakov, A.S. (1984) A variety of serpentine with a lattice transitional between lizardite and clinochrysotile, as a rock-forming mineral in Alpine-type ultramafic rocks. Doklady Earth Science Sections, 278, 133–137.

Varlakov, A.S. and Guriev, S.A. (1985) Ophites and Povlen-chrysotile in ultrabasic rocks. IzvestiaAkademie NAUK SSSR, 12, 72–81 (in Russian).

Viti, C. and Mellini, M. (1996) Vein antigorites from Elba Island, Italy. European Journal of Mineralogy, 8, 423–434.

Viti, C. and Mellini, M. (1997) Contrasting chemical compositions in coexisting lizardite and chrysotile from Elba veins. European Journal of Mineralogy, 9, 585–596.

——— (1998) Mesh textures and bastites in the Elba retrograde serpentinites. European Journal of Mineralogy, 10, 1341–1359.

Yada, K. and Wei, L. (1987) Polygonal microstructures of Povlen chrysotile observed by high resolution electron microscopy. Abstracts Sixth Meeting of the European Clay Groups (Seville), 596–597.

Zussman, J. and Brindley, G.W. (1957) Electron diffraction studies of serpentine minerals. American Mineralogist, 42, 133–153.

Manuscript received March 28, 2006
Manuscript accepted October 23, 2006
Manuscript handled by Warren Huff